Optics Letters

Multi-exposure interferometric diffusing wave spectroscopy

Wenjun Zhou,[1] Mingjun Zhao,[1] Oybek Kholiqov,[1] and Vivek J. Srinivasan[1,2,3,*]

[1]Department of Biomedical Engineering, University of California Davis, Davis, California 95616, USA
[2]Department of Ophthalmology, NYU Langone Health, New York, New York 10016, USA
[3]Department of Radiology, NYU Langone Health, New York, New York 10016, USA
*Corresponding author: vjsriniv@ucdavis.edu

Received 21 April 2021; revised 28 June 2021; accepted 26 July 2021; posted 29 July 2021 (Doc. ID 427746); published 7 September 2021

We present multi-exposure interferometric diffusing wave spectroscopy (MiDWS), which measures brain blood flow index (BFI) continuously and non-invasively. MiDWS employs interferometry to detect low light levels, probing the optical field autocorrelation indirectly by varying the sensor exposure time. Here MiDWS is compared with conventional interferometric diffusing wave spectroscopy and speckle contrast optical spectroscopy in phantoms. Notably, the MiDWS approach enables the use of low frame rate, two-dimensional complementary metal–oxide semiconductor cameras in a short exposure time regime, where detector noise greatly exceeds the sample photon count. Finally, we show that MiDWS can monitor the BFI simultaneously at two source-collector separations (1 and 3 cm) on the adult human head on a single camera, enabling the use of superficial signal regression techniques to improve brain specificity.

https://doi.org/10.1364/OL.427746

Cerebral blood flow (CBF) regulation is a part of normal brain function, and signals linked to CBF changes are useful proxies for brain activity. Yet, measuring CBF in adult humans currently requires high-end medical instrumentation [1]. Diffusing wave spectroscopy (DWS) and diffuse correlation spectroscopy (DCS) can quantify temporal fluctuations of diffuse light that traverses brain tissue, deriving a blood flow index (BFI) that serves as a surrogate for CBF [2,3]. However, since DWS/DCS measures coherent light fluctuations, the approach cannot appreciably benefit from incoherent summation of speckle intensity. Thus, for non-invasive measurements of the adult human brain at large source-collector (S-C) separations (i.e., $\geq$2.5 cm), DWS/DCS requires many expensive single photon counting channels [4]. While a multispeckle, 1024 channel DCS system was achieved with a single photon avalanche diode (SPAD) camera, S-C separations of this approach remain relatively limited to date [5,6]. Developed from multi-exposure speckle imaging [7], speckle contrast optical spectroscopy (SCOS) is an alternative method that uses two-dimensional (2D) sensors to quantify diffuse speckle contrast at one or more exposure times to estimate the BFI [8]. SPAD arrays [9,10], charged-coupled device cameras [11], and scientific complementary metal–oxide semiconductor cameras (CMOS) [12], have served as SCOS detectors. Although SCOS does not require single photon counting and achieves a higher signal-to-noise ratio (SNR) than DWS/DCS for the adult human head, brain specificity of state-of-the-art SCOS has not improved over conventional DWS/DCS, which remains the gold standard.

Recently, interferometric diffusing wave spectroscopy (iDWS) [13–15] has shown potential to overcome the performance-to-cost limit of conventional DWS/DCS, and related approaches have been proposed [16–18]. While iDWS originally used a one-dimensional (1D) CMOS sensor [13], interferometric detection of the BFI has also been realized with 2D CMOS sensors, based on holographic technology [17,18]. Unfortunately, S-C separations of 2D sensor-based interferometric methods have not yet reached that of even state-of-the-art SCOS. Additionally, obtaining the BFI from a single interferometric exposure requires concurrent measurements of sample power [18]. Detailed comparisons of BFI measurement techniques are included in Table S1 of Supplement 1.

Here we demonstrate a new near-infrared optical approach called multi-exposure iDWS (MiDWS), which measures the brain BFI continuously and non-invasively with 2D CMOS technology at 3 cm S-C separation. Previously, iDWS was demonstrated with a 1D CMOS sensor that rapidly samples the optical field on the microsecond scale with a short exposure time relative to the decorrelation time [13]. By contrast, in our proposed MiDWS approach, decorrelation during the exposure time is an asset, not a liability. Thus, MiDWS can employ 2D CMOS arrays with low frame rates, widely found in cell phones and other mass-produced devices, providing a low cost per pixel. In this Letter, we compare MiDWS and iDWS, and show that multi-channel MiDWS can monitor at multiple S-C separations with a MMF bundle and a single camera.

In conventional iDWS, interference between the static reference field, $\mathbf{E}_R$, and the dynamic complex sample field, $\mathbf{E}_S(t)$, within a single detector or pixel, can be simply expressed as [13]

$$I = |\mathbf{E}_R + \mathbf{E}_S(t)|^2 = |\mathbf{E}_R|^2 + |\mathbf{E}_S(t)|^2 + 2\mathrm{Re}\left\{\mathbf{E}_R^* \cdot \mathbf{E}_S(t)\right\}. \quad (1)$$

iDWS [13–15] rapidly samples fluctuations in the heterodyne signal, $2\mathrm{Re}\{\mathbf{E}_R^* \cdot \mathbf{E}_S(t)\}$, to quantify the normalized field autocorrelation $[g_1(\tau_d)]$. Instead, the MiDWS approach probes $g_1(\tau_d)$ by varying the sensor exposure time, T_{exp} [Fig. 1(a)]. The

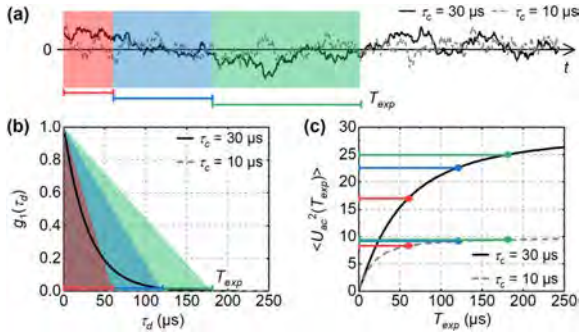

Fig. 1. MiDWS probes $g_1(\tau_d)$ with multiple exposure times (T_{exp}). (a) Temporal fluctuations of two heterodyne signals with decorrelation times of 30 and 10 μs, with different T_{exp} shaded. (b) Finite exposure is described mathematically in Eq. (4) by two-sided convolution of $g_1(\tau_d)$ with a T_{exp}-dependent triangular function (shaded). (c) $\langle U_{AC}^2(T_{exp})\rangle$ from Eq. (4), assuming $g_1(\tau_d) = \exp(-|\tau_d|/\tau_c)$, with $\tau_c = 30$ or 10 μs and $4\bar{\gamma}^2\bar{P}_S U_R = 1$. The colored horizontal bars indicate different T_{exp} in (a)–(c).

heterodyne fluctuation energy, U_{AC}, as a function of T_{exp}, is

$$U_{AC}(T_{exp}) = 2\mathrm{Re}\left\{\int_0^{T_{exp}} \mathbf{E}_R^* \cdot \mathbf{E}_S(t)\mathrm{d}t\right\}. \quad (2)$$

If the statistics of the real and imaginary parts of $\mathbf{E}_R^* \cdot \mathbf{E}_S(t)$ are identical, the mean squared $U_{AC}(T_{exp})$ can be written as

$$\langle U_{AC}^2(T_{exp})\rangle = 2\left\langle\left[\int_0^{T_{exp}} \mathbf{E}_R^* \cdot \mathbf{E}_S(t')\mathrm{d}t'\right]\left[\int_0^{T_{exp}} \mathbf{E}_R \cdot \mathbf{E}_S^*(t'')\mathrm{d}t''\right]\right\rangle, \quad (3)$$

where $\langle\cdot\rangle$ is assumed to denote time averaging over the integration time and/or pixel averaging, which are equivalent to ensemble speckle averaging assuming ergodicity. The field values, $\mathbf{E}_S$, at two times, t' and t'', are related by $\mathbf{E}_S(t'') = \mathbf{E}_S(t')g_1(t''-t') + \mathbf{N}_S(t', t'')[1 - g_1(t''-t')]$, where $\mathbf{N}_S(t', t'')$ is Gaussian speckle noise that is uncorrelated with $\mathbf{E}_S(t')$. Thus, Eq. (3) can be rewritten as

$$\begin{aligned}\langle U_{AC}^2(T_{exp})\rangle &= 2\left\langle\int_0^{T_{exp}}\int_0^{T_{exp}} |\mathbf{E}_R^* \cdot \mathbf{E}_S(t')|^2 g_1(t''-t')\,\mathrm{d}t''\mathrm{d}t'\right\rangle \\ &= 4\bar{\gamma}^2\bar{P}_S U_R \int_0^{T_{exp}} g_1(\tau_d)\left(1 - \frac{\tau_d}{T_{exp}}\right)\mathrm{d}\tau_d, \end{aligned} \quad (4)$$

where U_R is the reference count level [i.e., $U_R = \bar{P}_R(T_{exp})\,T_{exp}$], and $\bar{\gamma}$, $\bar{P}_S$, and $\bar{P}_R(T_{exp})$ are the time- and/or pixel-averaged mutual coherence degree [13], sample power, and reference power (assumed to vary with T_{exp}), respectively. Assuming an exponential $g_1(\tau_d)$ [Fig. 1(b)] and a constant reference count level [i.e., $\bar{P}_R(T_{exp}) = U_R/T_{exp}$] in Eq. (4), $\langle U_{AC}^2(T_{exp})\rangle$ increases with T_{exp}, eventually reaching a plateau [Fig. 1(c)]. This behavior is explained qualitatively by coherent averaging for short T_{exp} transitioning to incoherent averaging for long T_{exp}, and described mathematically as T_{exp}-dependent triangular weighting of $g_1(\tau_d)$ [Fig. 1(b)]. For a slower $g_1(\tau_d)$ decay, $\langle U_{AC}^2(T_{exp})\rangle$ would plateau at a higher level and longer T_{exp}. Hence, MiDWS can quantify sample dynamics.

First, the ability of MiDWS to quantify Brownian motion was validated against iDWS and SCOS. We modified a line-scan CMOS camera (spL4096-140km, Basler)-based iDWS system [15] with an 852 nm laser source (D2-100-DBR-852-HP1, Vescent Photonics), to implement all three modalities with different camera settings [Fig. 2(a)]. First, for MiDWS, 28 T_{exp} ranging from 10 μs to 1 ms were achieved by level triggering the camera with a 500 Hz counter signal with a variable duty cycle from the digital acquisition card (DAQ, PCIe-6363, NI). An electronic variable optical attenuator (VOA, V800A, Thorlabs), driven by an analog output which triggered the counter output [inset of Fig. 2(a)], varied reference power to ensure constant photon counts [i.e., $\bar{P}_R(T_{exp}) = U_R/T_{exp}$]. Second, for iDWS, heterodyne fluctuations were rapidly sampled with a fixed T_{exp} and 333 kHz rate, using the camera's free-run mode and a fixed reference power [15]. Third, for SCOS, measurements were performed at the same T_{exp} as MiDWS while blocking the reference arm. The camera region of interest (ROI) was set to 512 pixels for all modalities.

In MiDWS, for each T_{exp}, the basic analysis consists of temporal mean subtraction and calculation of the mean

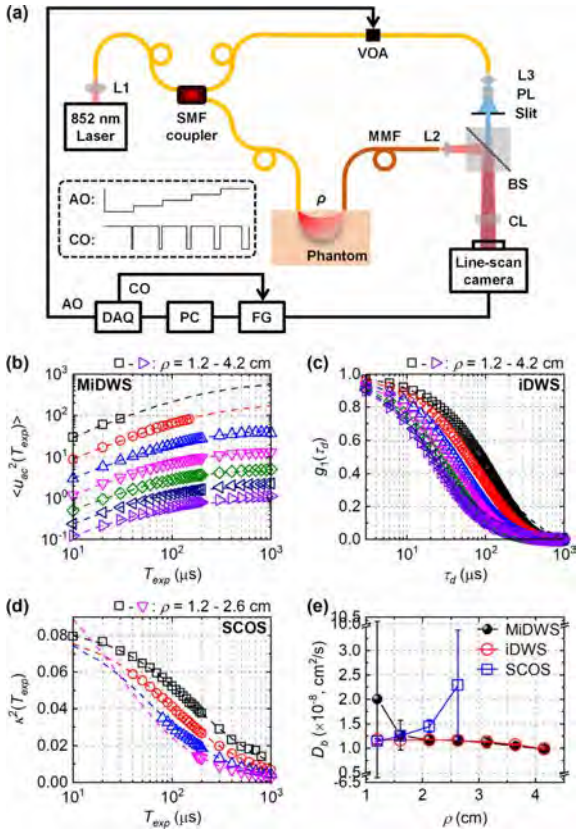

Fig. 2. Validation of MiDWS in phantoms with the setup in Ref. [15], modified to perform MiDWS, iDWS, and SCOS. (a) Schematic of the MiDWS system with a line-scan camera. The dashed frame shows a typical AO signal for modulating reference power, a CO signal for triggering camera exposure. ρ, S-C separation; VOA, variable optical attenuator; PL, Powell lens; BS, beam splitter; CL, cylindrical lens; L1, L2, and L3, spherical lens; DAQ, digital acquisition card; FG, frame grabber; PC, computer; AO, analog output; CO, counter output. (b)–(d) $\langle u_{ac}^2(T_{exp})\rangle$, $g_1(\tau_d)$, and $\kappa^2(T_{exp})$ for (b) MiDWS, (c) iDWS, and (d) SCOS, at different S-C separations. The dashed curves in (b)–(d) indicate corresponding fits. The integration times are 56, 2, and 56 s for $\langle u_{ac}^2(T_{exp})\rangle$, $g_1(\tau_d)$, and $\kappa^2(T_{exp})$ curves, respectively. (e) Fitted Brownian diffusion coefficients (D_b) from results in (b)–(d). The error bars indicate 95% confidence intervals.

squared heterodyne signal across all pixels. The latter computation is line-by-line or frame-by-frame, which obviates sampling faster than the decorrelation time. Heterodyne fluctuations consist of a signal and additive noise, which are considered as real, zero-mean, and mutually independent Gaussian random variables for each pixel. Thus, the noise-contaminated $\langle U_{AC+N}^2 \rangle$ can be corrected and normalized by taking $\langle u_{AC}^2 \rangle = (\langle U_{AC+N}^2 \rangle - \sigma_C^2 - \sigma_R^2 - \sigma_S^2)/U_R$, where σ_C^2, σ_R^2, and σ_S^2 are the noise variances of camera, reference, and sample backgrounds, respectively. Note that the normalization by U_R compensates for slight reference count variations with T_{exp}, which are not compensated for by the VOA. The three noise variances were estimated from separate background measurements (no reference or sample yielding σ_C^2, sample only yielding $\sigma_C^2 + \sigma_S^2$, and reference only yielding $\sigma_C^2 + \sigma_R^2$). Finally, for multi-exposure SCOS, a standard noise correction method was used for the squared temporal speckle contrast, $\kappa^2(T_{\text{exp}})$ [8] with the aforementioned background measurements.

Next, the relative abilities of the three methods to quantify Brownian diffusion coefficients were compared [Figs. 2(b)–2(d)] on an intralipid phantom with known optical properties ($\mu_s' = 6\,\text{cm}^{-1}$, $\mu_a = 0.05\,\text{cm}^{-1}$). For MiDWS, $\langle u_{AC}^2(T_{\text{exp}}) \rangle$ at S-C separations from 1.2 to 4.2 cm were calculated with a 10-line temporal mean subtraction (noise variances in Fig. S1 of Supplement 1) and fitted by Eq. (4) [Fig. 2(b)], where $4\bar{\gamma}^2 \bar{P}_S U_R$ was replaced with a single fitting parameter, and $g_1(\tau_d)$ was a semi-infinite homogenous DCS model [2,3]. MiDWS data corrupted by camera saturation caused by high $\bar{P}_S$ were removed from Fig. 2(b), and SCOS data biased by low SNRs (i.e., low $\bar{P}_S$) were excluded in Fig. 2(d). In Fig. 2(e), fitted Brownian diffusion coefficients (D_b) of MiDWS [Fig. 2(b)], iDWS [Fig. 2(c)], and SCOS [Fig. 2(d)] are compared. iDWS agrees with MiDWS at $\rho > 2$ cm, and SCOS agrees with MiDWS at $\rho < 1.5$ cm [Fig. 2(e)]. Deviations reflect underestimation of $\langle u_{AC}^2(T_{\text{exp}}) \rangle$ at $\rho < 2$ cm [Fig. 2(b)] and overestimation of $\kappa^2(T_{\text{exp}})$ at $\rho > 1.5$ cm [Fig. 2(d)]. Note that camera saturation and $\langle u_{AC}^2 \rangle$ underestimation were unique problems for the 1D camera setup due to the high $\bar{P}_S$. Thus, measuring $\langle u_{AC}^2(T_{\text{exp}}) \rangle$ is a viable alternative to directly measuring $g_1(\tau_d)$.

Next, to take advantage of the low pixel cost of 2D sensors, we built an MiDWS system with an area-scan CMOS camera (acA2040-180kmNIR, Basler) [Fig. 3(a)] for BFI monitoring in the adult human brain. The MiDWS system is also based on a Mach–Zehnder interferometer. In the sample arm, the source illuminates the scalp with a power of 50 mW and a spot size of >4 mm (adhering to the ANSI maximum permissible exposure) via a contact probe. Light is collected at 1 (superficial sensitivity) and 3 cm (superficial and deep sensitivity) S-C separations by two legs of a contact MMF bundle probe (FCA-840-FEA-2m, O-m6), and coherently enhanced by reference light. In the reference arm, a variable beam expander (BE052-B, Thorlabs), a beam shaper (πShaper, #36–649, Edmund Optics), and an anamorphic prism pair (PS875-B, Thorlabs) convert a circular Gaussian beam into an elliptical flat-top beam, which covers a camera ROI of ~1700 by 280 pixels with quasi-uniform reference intensity. A frame rate of 250 Hz, mainly limited by the ROI, was used for *in vivo* measurements. Finally, alternating T_{exp} of 47.7 and 197.7 μs was chosen to balance the trade-off between the SNR and specificity for the adult human brain [15]. A two-frame temporal mean subtraction was used (Section S4 of Supplement 1).

With this 2D MiDWS system, we investigated the optical BFI response of a 35-year-old man to voluntary apnea (VA), which is a coarse method of assessing cerebrovascular reactivity [15]. All experimental procedures and protocols involving human subject research were reviewed and approved by the UC Davis Institutional Review Board. End-tidal respiratory CO_2 was monitored by a capnometer (9004051, Smiths Medical) during VA [Fig. 3(b)]. A breath holding period of ~55 s was determined from the duration of absence of the respiratory CO_2 waveform. After resumption of breathing, an increase of end tidal CO_2 ($etCO_2$) of ~10 mmHg was observed. BFIs at both S-C separations were fitted from corresponding pairs of $\langle u_{AC}^2(T_{\text{exp}}) \rangle$. A heart rate (HR), estimated from a pulsatile BFI at 3 cm S-C separation [inset of Fig. 3(c)], agrees well with that of a pulse oximeter (3044, Smiths Medical) [Fig. 3(b)]. For noise correction, σ_R^2 was estimated as the contemporaneous reference count U_R times a proportionality constant (determined from reference background measurements), and σ_S^2 was assumed to be zero (due to low collected sample power per pixel) for *in vivo*

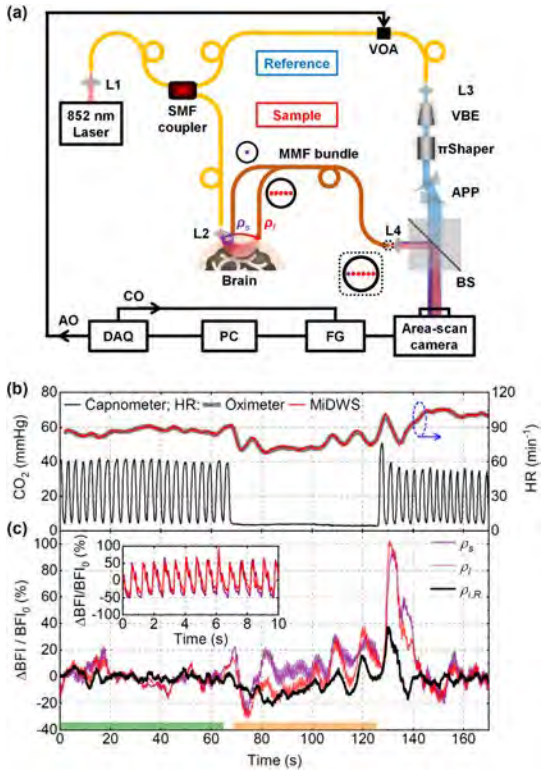

Fig. 3. *In vivo* MiDWS of the human brain. (a) Schematic of the MiDWS system with an area-scan 2D camera. A fiber bundle with legs of 1 and 5 MMFs (200 μm core diameter, 0.22 NA) collects light at short (ρ_s, purple) and long (ρ_l, red) S-C separations, respectively. The dotted frame indicates MMF bundle mapping. VBE, variable beam expander; APP, anamorphic prism pairs. Other components (L1-L4, BS, VOA, DAQ, FG, and PC) are described in Fig. 2(a). (b) Respiratory CO_2 waveform, monitored by a commercial capnograph, and heart rate (HR), measured by an oximeter (thick gray) and MiDWS (red), during VA. The blue dashed oval with arrow points to corresponding y axis. (c) Relative BFI changes at $\rho_s = 1$ cm (purple) and $\rho_l = 3$ cm (red), with 2 s integration time and 0.008 s sampling interval (Section S3 of Supplement 1). The superficial signal-regressed BFI change ($\rho_{l,R}$, black) better isolates the brain [19]. Inset: pulsatile BFI fluctuations with 0.096 s integration time at both S-C separations. The green and orange bars indicate the baseline (for estimating regression factor) and VA, respectively.

noise correction. Relative BFI changes show responses to VA for both S-C separations [Fig. 3(c)], which seem correlated to the systemic HR response [Fig. 3(b)]. A temporal correlation factor (regression factor) of ∼0.78 was estimated from the baseline BFIs (Section S5 of Supplement 1) [19]. The superficial signal-regressed 3 cm S-C separation BFI trace yielded a flatter baseline and a BFI increase of ∼37%, a reasonable CBF change for a ∼10 mmHg increase in $etCO_2$ [20], suggesting that 2D MiDWS can monitor the BFI in adults with high brain specificity.

A recurring theme in diffuse optics is the trade-off between the SNR (or light throughput) and brain specificity. The choice of T_{exp} for MiDWS represents a novel way to realize this trade-off. For direct $g_1(\tau_d)$ measurements, brain specificity can be enhanced by fitting early time lags and, as an extreme example, estimating the zero lag derivative [15]. Similarly, a MiDWS BFI measured from $\langle u_{ac}^2 \rangle$ at short T_{exp} can also achieve higher brain specificity, as the triangular weighting in Eq. (4) is confined to early lags. Yet, this strategy results in lower signal levels [Fig. 1(c)]. A T_{exp} several times longer than the decay time of $g_1(\tau_d)$ nearly maximizes the signal level [Fig. 1(c)]. Yet, this strategy reduces brain specificity by integrating over the long τ_d "tails" of g_1 [Eq. (4)], which arise from superficial light paths. A similar trade-off is also present in SCOS, which integrates over g_2, though g_2 has smaller tails than g_1. Hence, in addition to the S-C separation, T_{exp} should also be considered when evaluating and comparing systems based on MiDWS or SCOS.

To balance this SNR-brain specificity trade-off, this Letter used an S-C separation of 3 cm, and a relatively short T_{exp} of 47.7 μs, close to the decay time of $g_1(\tau_d)$ for a 3 cm S-C separation on the adult human head [15]. Our S-C separation is larger than other reported adult human brain BFI measurements with 2D cameras [6,9–12,18]. Even so, our T_{exp} are much smaller than the few millisecond scale typically used in SCOS [9–11]. The optical "gain" provided by the reference light is a key enabler of this short T_{exp}, in a region where the sample photon count is about three orders of magnitude smaller than the camera noise. However, the brain specificity of MiDWS has yet to approach that of iDWS [15], which achieved up to 5 cm S-C separation and accesses early (∼3 μs) time lags. Nonetheless, MiDWS benefits from inexpensive CMOS pixels on a 2D sensor, which can be allocated to short and long separation channels, improving brain specificity by signal regression.

The SNR of MiDWS can be affected by numerous factors, including the pixel rate (pixel number times frame rate) and pixel spatial correlation, T_{exp} values, and integration (total measurement) time [21]. For example, in phantom experiments, which did not fully optimize the MiDWS pixel rate, MiDWS estimates had larger error bars than did iDWS [Fig. 2(e)]. The low MiDWS pixel rate resulted from the MiDWS frame rate of 500 Hz, which was in turn limited by the 1 kHz modulation bandwidth of the VOA. Thus, a 1D camera with a low pixel count could not fully realize the advantages of MiDWS. On the other hand, with a larger 2D camera, the *in vivo* MiDWS system reached ∼70% of the pixel rate of a previous iDWS system [15]. The SNR of the *in vivo* MiDWS system was high enough for pulsatile BFI monitoring at 3 cm S-C separation, comparable to DCS/DWS [4]. Thus, enhancing the pixel rate with a large sensor is a critical way to improve MiDWS, particularly if the frame rate is limited. To improve brain specificity further, decreasing T_{exp} would require additional SNR improvements. Optimizing the setup to achieve a higher SNR will be crucial to improve MiDWS of the adult human brain.

In summary, an MiDWS method which quantifies sample dynamics by probing $g_1(\tau_d)$ with a varying sensor exposure is proposed, validated, and demonstrated in the adult human brain. *In vivo* results suggest that 2D camera MiDWS can improve the performance-to-cost of optical BFI measurements and, eventually, measure CBF and brain activation in novel settings.

Funding. National Institutes of Health (R01EB029747, R01EY031469); National Natural Science Foundation of China (62105315).

Disclosures. The authors declare no conflicts of interest.

Data Availability. Data underlying the results presented in this paper are not publicly available at this time but may be obtained from the authors upon reasonable request.

Supplemental document. See Supplement 1 for supporting content.

REFERENCES

1. S.-P. Peng, Y.-N. Li, J. Liu, Z.-Y. Wang, Z.-S. Zhang, S.-K. Zhou, F.-X. Tao, and Z.-X. Zhang, Neural Regen. Res. **11**, 1115 (2016).
2. T. Durduran and A. G. Yodh, NeuroImage **85**, 51 (2014).
3. E. Buckley, A. Parthasarathy, P. E. Grant, A. Yodh, and M. A. Franceschini, Neurophotonics **1**, 011009 (2014).
4. G. Dietsche, M. Ninck, C. Ortolf, J. Li, F. Jaillon, and T. Gisler, Appl. Opt. **46**, 8506 (2007).
5. E. Sie, H. Chen, E.-F. Saung, R. Catoen, T. Tiecke, M. Chevillet, and F. Marsili, Neurophotonics **7**, 035010 (2020).
6. W. Liu, R. Qian, S. Xu, P. C. Konda, J. Jönsson, M. Harfouche, D. Borycki, C. Cooke, E. Berrocal, Q. Dai, H. Wang, and R. Horstmeyer, APL Photonics **6**, 026106 (2021).
7. C. P. Valdes, H. M. Varma, A. K. Kristoffersen, T. Dragojevic, J. P. Culver, and T. Durduran, Biomed. Opt. Express **5**, 2769 (2014).
8. A. B. Parthasarathy, W. J. Tom, A. Gopal, X. Zhang, and A. K. Dunn, Opt. Express **16**, 1975 (2008).
9. T. Dragojević, J. L. Hollmann, D. Tamborini, D. Portaluppi, M. Buttafava, J. P. Culver, F. Villa, and T. Durduran, Biomed. Opt. Express **9**, 322 (2018).
10. T. Dragojević, J. L. Hollmann, E. E. Vidal Rosas, K. Pasquinelli, I. Cusini, J. P. Culver, F. Villa, and T. Durduran, in *Biophotonics Congress: Biomedical Optics*, OSA Technical Digest (2020), paper BTh3C.3.
11. R. Bi, Y. Du, G. Singh, J.-H. Ho, S. Zhang, A. B. Ebrahim Attia, X. Li, and M. Olivo, J. Biomed. Opt. **25**, 055003 (2020).
12. K. Murali and H. M. Varma, Biomed. Opt. Express **11**, 6699 (2020).
13. W. Zhou, O. Kholiqov, S. P. Chong, and V. J. Srinivasan, Optica **5**, 518 (2018).
14. W. Zhou, O. Kholiqov, and V. J. Srinivasan, "Interferometric technique for measuring cerebral blood flow using inexpensive CMOS sensors," U.S. patent applicationPCT/US2019/027546 (24October 2019).
15. W. Zhou, O. Kholiqov, J. Zhu, M. Zhao, L. L. Zimmermann, R. M. Martin, B. G. Lyeth, and V. J. Srinivasan, Sci. Adv. **7**, eabe0150 (2021).
16. M. Robinson, D. Boas, S. Sakadžic, M. A. Franceschini, and S. Carp, J. Biomed. Opt. **25**, 097004 (2020).
17. E. James and S. Powell, Biomed. Opt. Express **11**, 6755 (2020).
18. J. Xu, A. K. Jahromi, J. Brake, J. E. Robinson, and C. Yang, APL Photonics **5**, 126102 (2020).
19. N. Gregg, B. White, B. Zeff, A. Berger, and J. Culver, Front. Neuroenerg. **2**, 14 (2010).
20. H. Ito, I. Kanno, M. Ibaraki, J. Hatazawa, and S. Miura, J. Cereb. Blood Flow Metab. **23**, 665 (2003).
21. J. Xu, A. K. Jahromi, and C. Yang, APL Photonics **6**, 016105 (2021).